Carrier-concentration-dependent resonance frequency shift in a metamaterial loaded semiconductor

Seiji Myoga,[1] Tomohiro Amemiya,[2,*] Atsushi Ishikawa,[3] Nobuhiko Nishiyama,[1] Takuo Tanaka,[3] and Shigehisa Arai[1,2]

[1]*Department of Electrical and Electronic Engineering, Tokyo Institute of Technology, Tokyo 152-8552, Japan*
[2]*Quantum Nanoelectronics Research Center, Tokyo Institute of Technology, Tokyo 152-8552, Japan*
[3]*Metamaterial Laboratory, RIKEN, 2-1 Hirosawa, Wako, Saitama 351-0198, Japan*
**Corresponding author: amemiya.t.ab@m.titech.ac.jp*

Received March 6, 2012; revised May 30, 2012; accepted June 21, 2012;
posted June 22, 2012 (Doc. ID 163666); published July 25, 2012

We examined the electromagnetic responses of near-infrared metamaterials consisting of split-ring resonators fabricated on GaInAs semiconductor layers with different doping levels on an InP substrate. The inductance-capacitance (LC) resonances of the split-ring resonators could be controlled entirely from 52 to 63 THz by changing the carrier concentrations from 2.6×10^{18} to 2.7×10^{19} cm^{-3}. Our results show the feasibility of semiconductor-based tunable metamaterials. © 2012 Optical Society of America

OCIS codes: 160.3918, 130.5990, 260.5740.

1. INTRODUCTION

It is commonly recognized that every naturally occurring material interacts with an electric but not a magnetic field at high frequencies. This is because unpaired electron spins cannot follow the high-frequency field. The relative permeability of materials in nature is thus fixed to be unity in the optical and visible frequency regions.

The control of both permittivity and permeability would open up a new field for future communication technologies. For example, by controlling both permittivity and permeability it is possible in theory to achieve the sophisticated manipulation of light, including slowing, trapping, and storing light signals [1–4].

Metamaterials are artificial materials designed to have desired permittivity and permeability values that are never obtained in nature [5,6]. One of the promising methods for realizing metamaterials is in the use of a split-ring resonator (SRR) [7–11]. At the resonance frequency of SRRs, the inductive magnetic fields inside the ring generated by incident light change the effective permeability. Tuning electromagnetic response through the control of metamaterial properties (i.e., tunable metamaterials) [12] is the most indispensable application area in this field. A typical way to realize tunable metamaterials is to integrate a reconfigurable material into a metamaterial structure. Active tuning is then achieved by applying an external stimulus. GaAs-based modulators with SRRs [13–16] and metamaterial memories on a VO_2 film [17,18] are examples of such device prototypes, which operate at a frequency of 1–10 THz.

Realizing tunable metamaterials for higher frequencies (e.g., optical frequency) is also a promising challenge for future photonic devices. They must, by necessity, have the form of a compound semiconductor device that is compatible with other conventional photonic devices [19]. Recent researches for tunable metamaterials at optical frequencies [20,21], however, cannot meet this requirement because they normally use glass substrates, which are incompatible with other semiconductor-based photonic devices.

In this paper, we explored the effects of semiconductor carrier concentration on resonance tuning at around 60 THz (5 μm wavelength), bringing optical frequencies into reach for controlling the permeability in photonic devices. We examined the near-infrared responses of metamaterials consisting of the SRRs fabricated on semiconductor GaInAs layers with different doping levels for the realization of dynamic control of metamatrial's optical properties.

First, the device structure and its fabrication process are explained in Section 2. The operating characteristics of the device, including the transmission as a function of the polarization and wavelength of incident light, are also given in this section. Theoretical investigations of the measurement results are then presented in Section 3 using a finite-element method (FEM). Finally, Section 4 concludes the paper.

2. FABRICATION AND MEASUREMENTS

Our metamaterial device structure is shown in Fig. 1. The C-shaped SRR array was made on a GaInAs/InP wafer. The individual SRR mimics an inductance-capacitance (LC) circuit consisting of a capacitor with capacitance C (the gap) and a magnetic coil with inductance L (the rest of the ring). Coupling of the incident radiation to the LC circuit is possible if the electric field vector]\has a component perpendicular to the plates of the capacitor. Under this condition, a circulating current is induced in the coil, leading to a magnetic dipole moment normal to the SRR plane. Based on this simple LC circuit model, one can derive the effective magnetic permeability of an array of SRRs at the resonance frequency.

In the device, the gap of each SRR is gradually short-circuited with an increase of carrier concentration in the GaInAs layer. Consequently, the magnitude of the effective permeability in the SRR region changes. Therefore, using

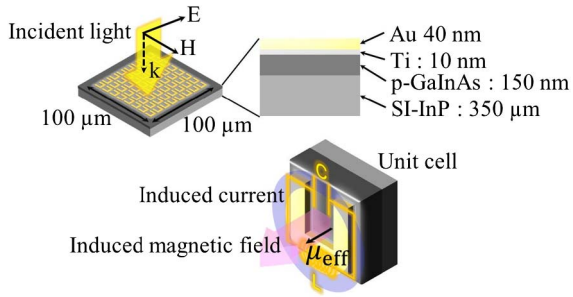

Fig. 1. (Color online) Schematic of the metamaterial sample consisting of a gold-based SRR array formed on doped-GaInAs/semi-insulating-InP.

carriers in the semiconductor layer excited by some external stimulus, the dynamic control of permeability is possible.

Toward the dynamic control of the metamaterial's responses by changing carrier concentrations in semiconductors, we fabricated a trial device consisting of SRRs fabricated on semiconductor GaInAs layers with different doping levels. All wafers consisted of an *n*- or *p*-GaInAs layer (150 nm thick) grown on a semi-insulating InP substrate by organometallic vapor phase epitaxy with different carrier concentrations, as summarized in Table 1. Silicon and zinc were used for *n*-type and *p*-type dopants.

The different steps of a fabrication process are depicted in Fig. 2. The process flow was as follows: A resist layer of polymethyl methacrylate (PMMA) was first spin-coated onto the GaInAs/InP wafer. Following spin coating, electron beam lithography was used to write the desired SRR array patterns onto the resist for the lift-off process and metal patterns were formed by evaporation. Figure 3 shows oblique scanning electron microscope images of the 400×400 nm (outer size of the square SRR ring) SRR array fabricated according to this procedure. The SRRs were made of 10 nm thick titanium and 40 nm thick gold. The dimensions of each individual SRR were designed to study resonance frequency shifts at around 60 THz (5 μm wavelength).

Figure 4 shows the transmission spectra of *n*-doped samples with 400×400 nm SRRs, measured using a Fourier-transform infrared (FTIR) spectrometer with a microscope *(JASCO FT/IR-6300FV)*. In this measurement, in order to clarify the effect of the interaction, we took the ratio of the transmission intensity of the experimental region (with SRRs) and that of a reference region (without SRRs) on the same wafer. (Note that the transmission coefficient surpasses 1 in measuring end because an FTIR detector is not sensitive in this region.) For incident light with an electric field vector perpendicular to the SRR gap, two distinct resonances were clearly visible [Fig. 4(a)]. The two principal types of resonance are usually known as the LC resonance at lower (around 60 THz) frequencies, and the plasmon or Mie resonance at higher (around 120 THz) frequencies. The fundamental LC resonance mode is caused by the inductance and capacitance of the SRRs—inductance is achieved by the ring structure, and capacitance occurs across the gap of the split. On the other hand, Mie resonance comes from a particle-plasmon resonance in the metal structure. Figure 4(a) implies that the electric field can couple to the capacitance of the SRR and induce a circulating current in the coil, leading to a pronounced magnetic response in the transmission spectra at around 60 THz. This magnetic resonance is termed as electric excitation of the magnetic resonance [22]. In contrast, when the electric field vector was rotated by 90° [Fig. 4(b)], the magnetic resonance disappeared because the electric field cannot couple to the SRR, leaving only the Mie resonance of the SRR at around 120 THz. More importantly, for both LC and Mie resonances, a clear blueshift in resonance frequency was observed as the doping level of the GaInAs layer increased. The LC resonances shifted monotonically from 52 to 63 THz when the carrier concentrations changed from 2.6×10^{18} to 2.7×10^{19} cm^{-3}. This shift in resonance frequency with carrier concentration may be also achieved by electrical injection for the dynamic tuning of the metamaterial's optical properties.

We also measured the relationship between the resonance frequency and dimensions of the SRRs. Table 1 shows the corresponding dimensions of the SRRs in nanometers. Figures 5 and 6 show the (a) LC and (b) Mie resonance frequencies of devices with different SRR dimensions as a function of carrier concentration of the *n*- and *p*-GaInAs layer, respectively. The polarization was perpendicular to the SRR gap. With increasing SRR size, an enhanced internal reactance reduced the resonant frequency that is determined by the geometrical capacitance and inductance of the structure. For every size of the SRR, the blueshift in resonance frequency was observed as the doping level of the GaInAs layer increased. This clearly shows that the resonance frequency can be controlled by varying the carrier concentration. To understand in detail these experimental results, numerical investigations using an FEM were pursued.

3. SIMULATION ANALYSIS

In this section, we performed simulations of our samples with different doping levels. The resonance shift occurs because a resistance and a capacitance within the split gap are influenced by the carrier concentration in the GaInAs

Table 1. Parameters Used in Experiments

Sample No.	Size[a]	Width[a]	Pitch Size	Substrate Doping Type	Doping Level
1	400×400	100	600	*n*	a: 2.6×10^{18}
2	600×600	100	900	*n*	b: 4.1×10^{18}
3	800×800	100	1200	*n*	c: 1.1×10^{19}
4	1000×1000	100	1500	*n*	d: 2.7×10^{19} (cm^3)
5	400×400	100	600	*p*	a: 1.9×10^{18}
6	600×600	100	900	*p*	b: 1.2×10^{19}
7	800×800	100	1200	*p*	c: 2.6×10^{19} (cm^3)
8	1000×1000	100	1500	*p*	

[a]The gap length is automatically determined when we set the size (outer size of the square SRR ring) and width of the SRR.

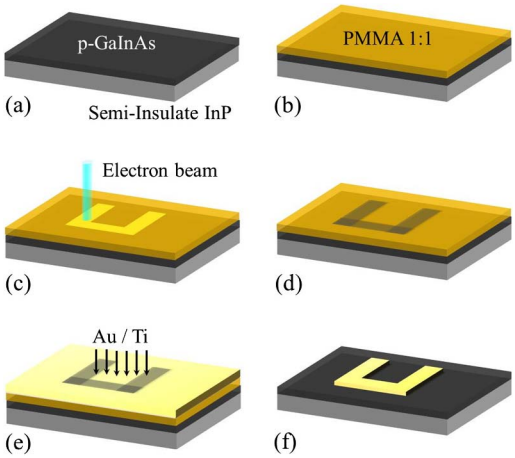

Fig. 2. (Color online) Fabrication process: (a) initial GaInAs/InP layer, (b) spin coating of PMMA, (c) electron-beam writing of the desired structure, (d) development, (e) evaporation of titanium and gold, and (f) lift-off.

layer. To describe the dispersive properties of the semiconductor GaInAs, we use the free-carrier absorption model [23]. This model is valid throughout the frequency range of interest because the mean free path in GaInAs (250 nm) is longer than an average travel distance for each electron accelerated by an electric field of light at 30–60 THz. Using these dispersion curves, we qualitatively calculate the magnetic response of the devices and present a principle for resonance frequency shift control in the device. This theoretical prediction is compared to the experimental results from the viewpoint of magnetic response.

A. GaInAs Dielectric Constant and Carrier Concentration

First, the dielectric function of the GaInAs layer at different doping levels was calculated because the magnetic response of the SRRs strongly depends on the conduction characteristics of the semiconductor layer. The permittivity and electrical conductivity of semiconductor materials as a function of the frequency f and carrier concentration N can be derived from the equation of motion for free carriers given by

$$\varepsilon(f,N)=\varepsilon_0\varepsilon_r\left\{1-\frac{[\omega_p(N)\tau(N)]^2}{1+[2\pi f\tau(N)]^2}\right\}, \tag{1}$$

$$\sigma(f,N)=\frac{\sigma_0(N)}{1+[2\pi f\tau(N)]^2}, \tag{2}$$

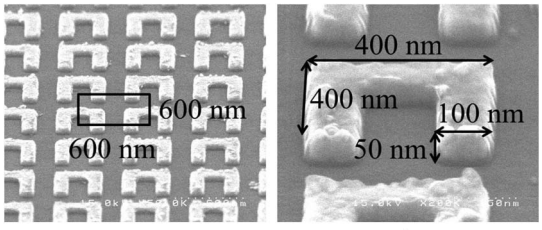

Fig. 3. (a) Scanning electron micrograph of a split-ring array with a total area of 100×100 μm^2; (b) enlarged oblique view of an individual split ring.

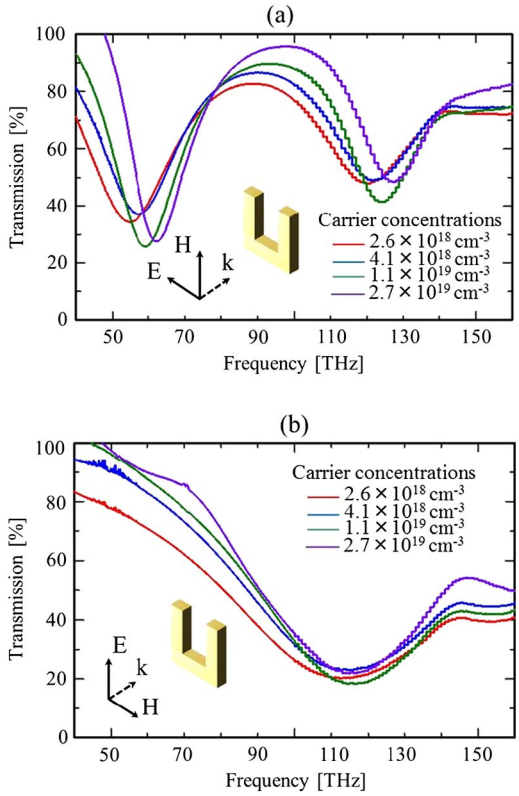

Fig. 4. (Color online) Normal-incidence transmittance spectra for the (a) horizontal and (b) vertical polarizations, measured with different carrier concentrations of the n-GaInAs layer.

where ε_0 and ε_r are the vacuum and static permittivity, respectively. Here $\varepsilon(f,N)$ in the Eq. (1) means the real part of the complex permittivity. On the other hand, the imaginary part of the complex permittivity can be obtained from $\sigma/\omega\varepsilon_0$ using σ in the Eq. (2). $\omega_p^2(N)=Nq^2/\varepsilon_0\varepsilon_r m^*$ is the plasma frequency. $\tau(N)=m^*\mu_{e,h}(N)/q$ is the mean free time. $\sigma_0(N)=q\mu_{e,h}(N)N$ is the static electric *conductivity*. m^* is the effective mass. The electron mobilities $\mu_e(N)$ are 3430 $cm^2\,V^{-1}\,s^{-1}$,

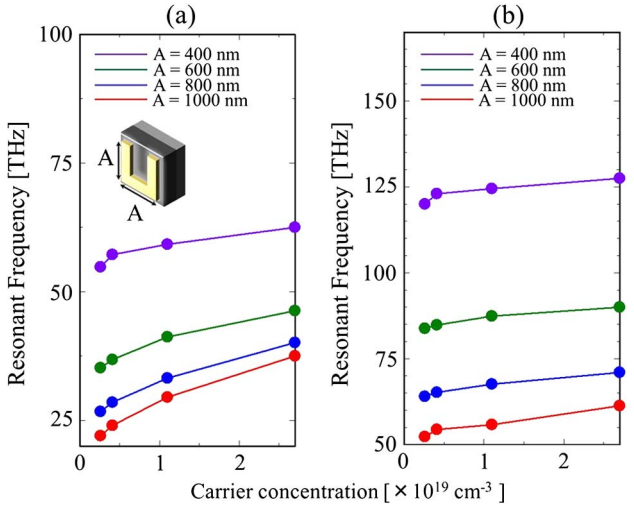

Fig. 5. (Color online) Resonance frequency as a function of carrier concentrations of the n-GaInAs layer for the (a) LC resonance and (b) Mie resonance, measured with an incident electric field vector perpendicular to the SRR gap.

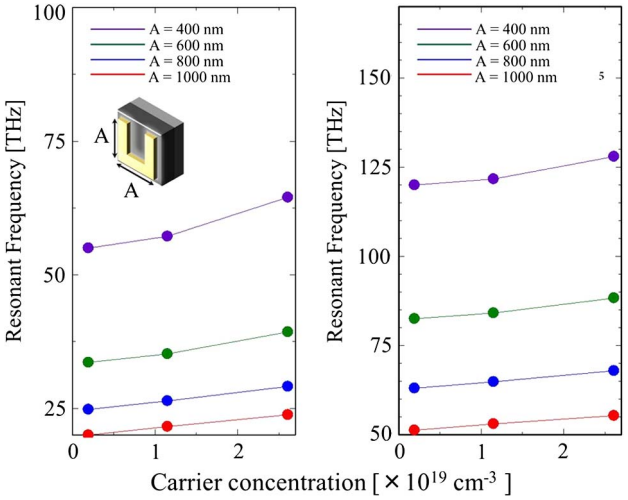

Fig. 6. (Color online) Resonance frequency as a function of carrier concentrations of the p-GaInAs layer for (a) LC resonance and (b) Mie resonance, measured with an incident electric field vector perpendicular to the SRR gap.

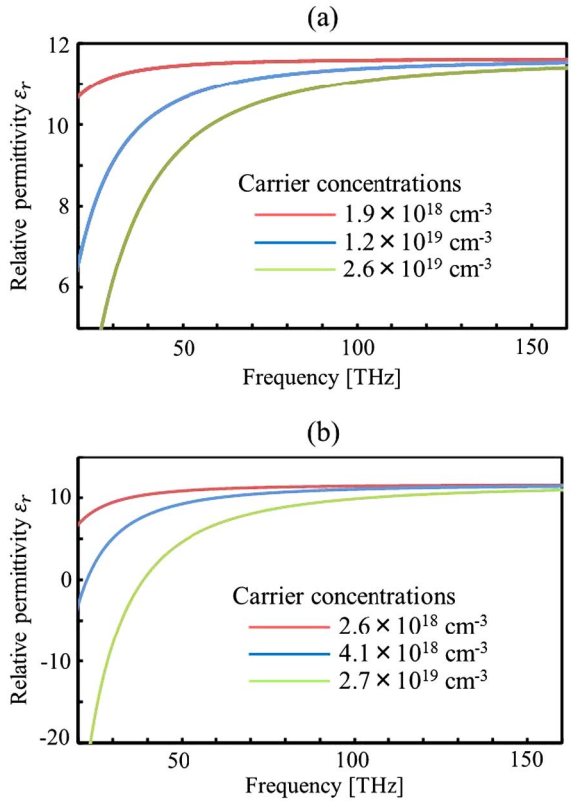

Fig. 7. (Color online) Real part of permittivity for (a) p-GaInAs and (b) n-GaInAs as a function of frequency. The carrier concentration N is a tuning parameter.

2740 $cm^2 V^{-1} s^{-1}$, 2600 $cm^2 V^{-1} s^{-1}$, and 1650 $cm^2 V^{-1} s^{-1}$ at carrier concentrations of 2.6×10^{18}, 4.1×10^{18}, 1.1×10^{19}, and 2.7×10^{19} cm^{-3}, respectively. The hole mobilities $\mu_h(N)$ are much smaller, having the values 110 $cm^2 V^{-1} s^{-1}$, 76 $cm^2 V^{-1} s^{-1}$, and 60 $cm^2 V^{-1} s^{-1}$ at carrier concentrations of 1.9×10^{18}, 4.1×10^{18}, and 2.6×10^{19} cm^{-3}, respectively. These electron and Hall mobilities were actually measured by Hall measurement. We measured the values of the above by Hall measurement. $\varepsilon(f, N)$ of Eq. (1) shows the real part of the complex permittivity, and you can obtain the imaginary part to calculate $\sigma/\omega\varepsilon_0$ using the Eq. (2).

Figures 7(a) and 7(b) show the calculated real part of the relative permittivity as a function of frequency for n-GaInAs and p-GaInAs, respectively. Carrier concentration N is a tuning parameter. Within the framework of the above model, the complex permittivity (or conductivity) and consequently all the optical parameters are fully characterized by two frequencies: the plasma frequency $\omega_p(N)$ and the relaxation rate $1/\tau(N)$. In general, $1/\tau(N) \ll \omega_p(N)$. As the frequency increases, the real part of the permittivity first increases sharply with ω^2 and then saturates above the plasma frequency. The relative permittivity decreases as the carrier concentration increases. This trend becomes more significant at longer wavelengths primarily owing to the blueshift of the plasma angular frequency with the increase of the carrier concentration, as derived from $\omega_p^2(N) = Nq^2/\varepsilon_0\varepsilon_r m^*$. Note that an imaginary part of the relative permittivity becomes larger with an increase of the carrier concentration. This change is relatively small (= 0.4) compared to that of the real part (= 5.4) at around 60 THz. Therefore, the resonant-frequency shift in this study is mainly induced by the real part change of permittivity in GaInAs.

There are two main factors that greatly affect the resonant frequency of the SRR in our samples. The first factor is the dissipation due to the substrate free carrier absorption within the split gap. The second factor, most dominant in our device, is the fringing capacitance within the split gap. The capacitance is related to the dielectric function of the semiconductor substrate due to fringing of field lines into the material. When the carrier concentration of the semiconductor substrate changes, the resulting capacitance change shifts the resonant frequency. As stated above (see Fig. 7), the real part of the dielectric function for GaInAs decreases as the carrier concentration increases. A decrease of the real component of the substrate dielectric function will decrease the capacitance within the split gap, and therefore shift the resonance to a higher frequency (or shorter wavelength). This is the principle for controlling of the resonance frequency in the device.

B. Transmission Characteristic

Using the calculated dielectric function of the GaInAs layer, the transmission characteristics of the device shown in Fig. 1 were estimated using the commercial software package *COMSOL Multiphysics* based on FEM. Considering the mutual interactions of each SRR, the electromagnetic field over a cubic unit cell consisting of a 3×3 gold SRR array on GaInAs/InP was calculated. We assumed perfect electric conductor and perfect magnetic conductor boundary conditions between unit cells in order to stimulate transverse electromagnetic plane wave propagation in the z direction. In the simulation, the conductivity of the metal was defined by the Drude model [24], and that for the III-V semiconductors with free carriers was defined using the theory in the previous section.

Figure 8(a) shows the simulated transmission spectra of a structure having the same structure as that for experimental sample 1 (see Table 1 for sample 1), where the polarization direction of the excitation light is perpendicular to the gap. In this simulation, we took the ratio of the transmission intensity of the device with SRRs and that of a GaInAs/InP

substrate, which was the same condition as the measurements. Two transmission minima for both LC and Mie resonances are observed in the near-infrared range. A clear blueshift of the resonance is also observed with an increase in carrier concentration of the GaInAs layer, consistent with the experimental observations shown in Fig. 4(a).

We also calculated the distribution of the magnetic field around the SRR at both of the LC and Mie resonance frequencies, as illustrated in Figs. 8(b) and 8(c). At the LC resonance frequency, the magnetic field intensity in the z direction is strongly induced inside the ring because an induced circular current flows in an individual ring through the gap capacitance, as shown in Fig. 8(b). On the other hand, at the Mie resonance frequency, the magnetic field intensity is strong outside of the ring due to plasmonic electron oscillation in the SRR arms along the direction of the incident electric field [see Fig. 8(c)].

Compared with the measured transmission spectra [Fig. 4(a)], the calculated transmission spectra [Fig. 8(a)] exhibited stronger and sharper resonances. The reason for these is explained as follows. In the simulation, the metal conductivity is defined by the Drude model with a scattering frequency of the bulk metal. The actual scattering frequency, however, is different from that found in the bulk because additional scattering effects (e.g., roughness scattering at the interface between the metal thin film structure and GaInAs layer) must be considered. However, it is difficult to quantify the actual interfacial condition between the Au/Ti thin film and GaInAs in our device, so we used a simple Drude model with a scattering frequency of the bulk metal.

From the theoretical expectations of the transmission spectra shown in Fig. 8(a), we extracted the constitutive parameter change induced by different doping levels in the device. Figures 9(a) and 9(b) show the real parts of the retrieved effective permittivity and permeability, respectively, calculated from 50 to 75 THz for incident light polarization direction perpendicular to the gap (see [25,26] for the retrieval procedure). The permittivity and permeability exhibit a strong and sharp antiresonance [27] at ~60 THz (corresponding to the LC resonance), and the real part of the relative permeability changes from −3.0 to 3.5 around this frequency. When the carrier concentration of the GaInAs layer is increased 2.6×10^{18} to 2.7×10^{19} cm^{-3}, the effective permeability at 63 THz changes from −1.0 to 3.0. A retrieved imaginary part of the relative permittivity (or permeability) also changes from −3.5 to 1.0 (or −1.0 to 3.5) in the vicinity of the resonant frequency. The imaginary parts of the constitutive parameters exhibited a blueshift as the doping level of the GaInAs layer increased.

This result suggests that there is a possibility to realize tunable metamaterials by changing the carrier concentrations in the semiconductor layer. Toward actual dynamic control, there are mainly two promising ways to control carrier concentrations in our device. One is to apply bias voltage in MOSFET-like structures; the other is to use an exciting light beyond bandgap energy of semiconductor. Using the

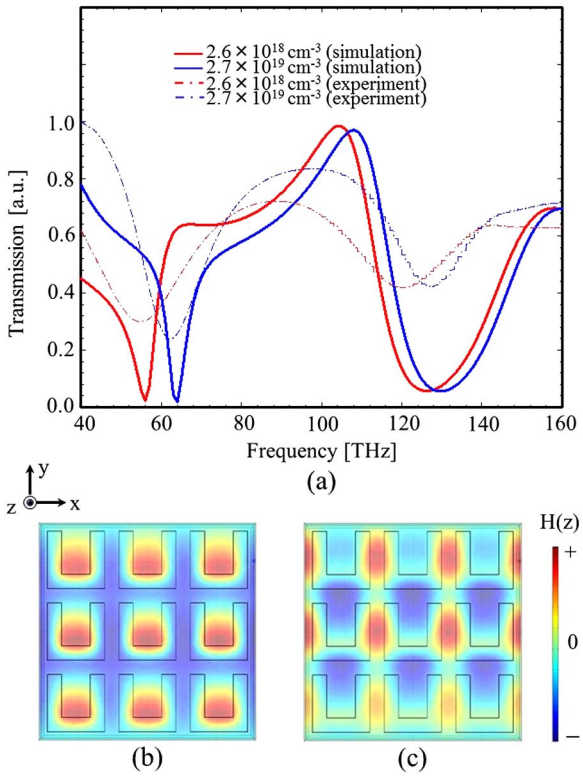

Fig. 8. (Color online) (a) Calculated transmission spectra of device having almost the same structure as that of experimental sample 1, where the polarization direction of the excitation light is perpendicular to the gap. Measurement results are also plotted. Calculated distributions of magnetic field (z direction) in the SRR array at (b) LC and (c) Mie resonance frequencies.

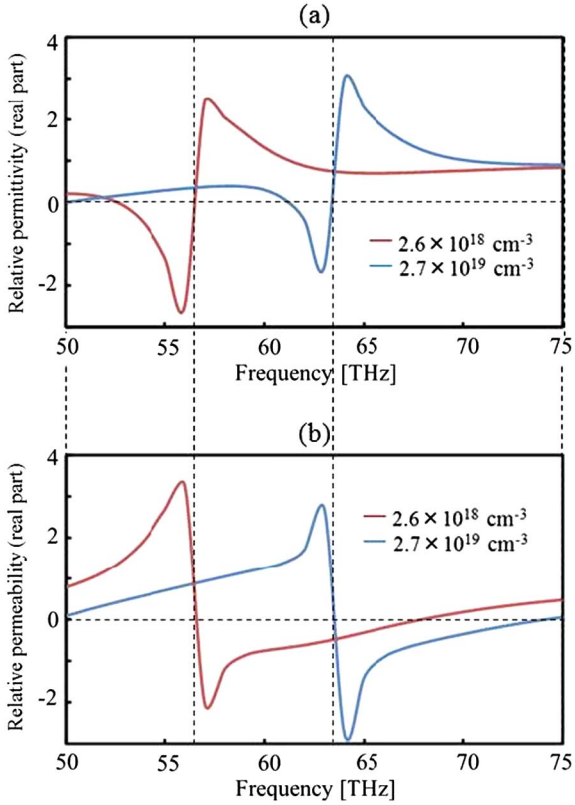

Fig. 9. (Color online) Retrieved real part of relative (a) permittivity and (b) permeability as a function of frequency, calculated for device having almost the same structure as that of experimental sample 1. The carrier concentration N is a tuning parameter.

above-mentioned method, we can realize flexible and simple tuning of the metamaterial rather than changing the dimensions of the metamaterial structure itself.

4. CONCLUSION

We have demonstrated the near-infrared responses of metamaterials consisting of SRRs fabricated on semiconductor GaInAs layers with different doping levels on an InP substrate for the realization of controlling the metamaterial's optical properties. From transmission spectra of the fabricated metamaterials, a clear blueshift of a resonance frequency was observed as the doping level of the GaInAs layer increased. LC resonances shifted monotonically from 52 to 63 THz when the carrier concentrations changed from 2.6×10^{18} to 2.7×10^{19} cm^{-3}, opening up the possibility of electrical tuning of metamaterial properties. Our results show the feasibility of semiconductor-based tunable metamaterials.

ACKNOWLEDGMENTS

This research was financially supported by the Ministry of Education, Culture, Sports, Science and Technology (MEXT), Japan, and the Japan Society for the Promotion of Science (JSPS) under Grants-in-Aid for Scientific Research (19002009, 22360138, 21226010, and 23760305).

REFERENCES

1. K. L. Tsakmakidis, A. D. Boardman, and O. Hess, "'Trapped rainbow' storage of light in metamaterials," Nature **450**, 397–401 (2007).
2. T. Jiang, J. Zhao, and Y. Feng, "Stopping light by an air waveguide with anisotropic metamaterial cladding," Opt. Express **17**, 170–177 (2009).
3. E. I. Kirby, J. M. Hamm, K. L. Tsakmakidis, and O. Hess, "FDTD analysis of slow light propagation in negative-refractive-index metamaterial waveguides," J. Opt. A: Pure Appl. Opt. **11**, 114027 (2009).
4. W. T. Lu, Y. J. Huang, B. D. F. Casse, R. K. Banyal, and S. Sridhar, "Storing light in active optical waveguides with single-negative materials," Appl. Phys. Lett. **96**, 211112 (2010).
5. S. A. Ramakrishna, "Physics of negative refractive index materials," Rep. Prog. Phys. **68**, 449–521 (2005).
6. C. M. Soukoulis, S. Linden, and M. Wegener, "Negative refractive index at optical wavelengths," Science **315**, 47–49 (2007).
7. T. J. Yen, W. J. Padilla, N. Fang, D. C. Vier, D. R. Smith, J. B. Pendry, D. N. Basov, and X. Zhang, "Terahertz magnetic response from artificial materials," Science **303**, 1494–1496 (2004).
8. S. Linden, C. Enkrich, M. Wegener, J. Zhou, T. Koschny, and C. M. Soukoulis, "Magnetic response of metamaterials at 100 terahertz," Science **306**, 1351–1353 (2004).
9. S. Linden, C. Enkrich, G. Dolling, M. W. Klein, J. Zhou, T. Koschny, C. M. Soukoulis, S. Burger, F. Schmidt, and M. Wegener, "Photonic metamaterials: magnetism at optical frequencies," IEEE J. Sel. Top. Quantum Electron. **12**, 1097–1105 (2006).
10. A. Ishikawa, T. Tanaka, and S. Kawata, "Frequency dependence of the magnetic response of split-ring resonators," J. Opt. Soc. Am. B **24**, 510–515 (2007).
11. A. Ishikawa, T. Tanaka, and S. Kawata, "Magnetic excitation of magnetic resonance in metamaterials at far-infrared frequencies," Appl. Phys. Lett. **91**, 113118 (2007).
12. Q. Zhao, L. Kang, B. Du, B. Li, J. Zhou, H. Tang, X. Liang, and B. Zhang, "Electrically tunable negative permeability metamaterials based on nematic liquid crystals," Appl. Phys. Lett. **90**, 011112 (2007).
13. W. J. Padilla, A. J. Taylor, C. Highstrete, M. Lee, and R. D. Averitt, "Dynamical electric and magnetic metamaterial response at terahertz frequencies," Phys. Rev. Lett. **96**, 107401 (2006).
14. H. T. Chen, W. J. Padilla, J. M. O. Zide, A. C. Gossard, A. J. Taylor, and R. D. Averitt, "Active terahertz metamaterial devices," Nature **444**, 597–600 (2006).
15. X. L. Xu, B. G. Quan, C. Z. Gu, and L. Wang, "Bianisotropic response of microfabricated metamaterials in the terahertz region," J. Opt. Soc. Am. B **23**, 1174–1180 (2006).
16. H. T. Chen, W. J. Padilla, J. M. O. Zide, S. R. Bank, A. C. Gossard, A. J. Taylor, and R. D. Averitt, "Ultrafast optical switching of terahertz metamaterials fabricated on ErAs/GaAs nanoisland superlattices," Opt. Lett. **32**, 1620–1622 (2007).
17. T. Driscoll, S. Palit, M. M. Qazilbash, M. Brehm, F. Keilimann, B. G. Chae, S. J. Yun, H. T. Kim, S. Y. Cho, N. M. Jokerst, D. R. Smith, and D. N. Basov, "Dynamic tuning of an infrared hybrid-metamaterial resonance using vanadium dioxide," Appl. Phys. Lett. **93**, 024101 (2008).
18. T. Driscoll, H. T. Kim, B. G. Chae, B. J. Kim, Y. W. Lee, N. M. Jokerst, S. Palit, D. R. Smith, M. D. Ventra, and D. N. Basov, "Memory metamaterials," Science **325**, 1518–1521 (2009).
19. L. A. Coldren, S. C. Nicholes, L. Johansson, S. Ristic, R. S. Guzzon, E. J. Norberg, and U. Krishnamachari, "High performace InP-based photonic ICs—a tutorial," J. Lightwave Technol. **29**, 554–570 (2011).
20. Z. L. Samson, K. F. MacDonald, F. D. Angelis, B. Gholipour, K. Knight, C. C. Huang, E. D. Fabrizio, D. W. Hewak, and N. I. Zheludev, "Metamaterial electro-optic switch of nanoscale thickness," Appl. Phys. Lett. **96**, 143105 (2010).
21. K. M. Dani, Z. Ku, P. C. Upadhya, R. P. Prasankumar, A. J. Taylor, and S. R. J. Brueck, "Ultrafast nonlinear optical spectroscopy of a dual-band negative index metamaterial all-optical switching device," Opt. Express **19**, 3973–3983 (2011).
22. N. Katsarakis, G. Konstantinides, A. Kostopoulos, R. S. Penciu, T. F. Gundogdu, M. Kafesaki, and E. N. Economou, "Magnetic response of split-ring resonators in the far-infrared frequency regime," Opt. Lett. **30**, 1348–1350 (2005).
23. M. Shirao, Y. Numajiri, R. Yokoyama, N. Nishiyama, M. Asada, and S. Arai, "Preliminary experiment on direct media conversion from a 1.55 μm optical signal to a sub-terahertz wave signal using photon-generated free carriers," Jpn. J. Appl. Phys. **48**, 090203 (2009).
24. P. B. Johnson and R. W. Christy, "Optical constants of the noble metals," Phys. Rev. B **6**, 4370–4379 (1972).
25. D. R. Smith, S. Schultz, P. Markos, and C. M. Soukoulis, "Determination of effective permittivity and permeability of metamaterials from reflection and transmission coefficients," Phys. Rev. B **65**, 195104 (2002).
26. X. Chen, T. M. Grzegorczyk, B. I. Wu, J. Pacheco, Jr., and J. A. Kong, "Robust method to retrieve the constitutive effective parameters of metamaterials," Phys. Rev. E **70**, 016608 (2004).
27. T. Koschny, P. Markos, D. R. Smith, and C. M. Soukoulis, "Resonant and antiresonant frequency dependence of the effective parameters of metamaterials," Phys. Rev. E **68**, 065602 (2003).